Digest Journal of Nanomaterials and Biostructures Vol. 19, No. 4, October-December 2024, p. 1677-1691

Investigation of the impact of transition metals (TM = Fe, Co, Ni) doping on the optoelectronic properties of tin dioxide SnO_2: first-principles analysis

J. Mhalla [a,*], I. Benaicha [a], Y. Qachaou [a], A. Yousfi [a], E. Laghchim [a], A. Fahmi [a], M. Lharch [a], K. Nouneh [a], A. Qachaou [a], M. Fahoume [a]
[a] *Materials Physics and Subatomic Laboratory, Department of Physics, Faculty of Science, Ibn Tofail University, Kenitra Morocco*

In this paper, we applied the density functional theory method, within the framework of GGA+U methods, to study the optoelectronic properties of undoped tin dioxide SnO_2. The effect of substitutional doping of transition metals (TM) in Sn-site on these properties was also investigated in $Sn_{0.92}TM_{0.08}O_2$ with TM = Fe, Co, Ni. Initially, we studied the Hubbard parameters U and the starting spin polarization to determine their optimal values. From the band structures, $Sn_{0.92}TM_{0.08}O_2$ appears to be a dilute magnetic semiconductor (DMS) with a direct bandgap. Our analysis of the total density of states revealed variations in the bandgap and Fermi level. Additionally, we explored the optical properties of these compounds in the UV, visible light, and infrared regions IR, observing a decrease in peak intensity and a shift from the IR to the UV-visible region. These findings align well with experimental studies and aim to provide interpretations and guidelines for future experimental work.

(Received August 27, 2024; Accepted November 1, 2024)

Keywords: First-principles calculation, TM-doped SnO2, Transparent conducting oxide, Electronic properties, Optical properties

1. Introduction

Over the last ten years, extensive research has focused on the use of nano-sized semiconductors. In the form of thin films, these semiconductors have enabled the integration of thousands of components, leading to the miniaturization of devices used in various technological applications. Examples include light-emitting diodes [1,2], photocatalysis [3], transparent electrodes in solar cells [4–6], and optoelectronic devices [7,8]. Transparent conducting oxides (TCOs) are a notable category of these semiconductors, playing a major role in the rapid development of these applications.

Among TCOs, tin dioxide (SnO_2), stands out as a highly versatile material. It has been extensively researched for its significant role in various technological applications. SnO_2 exhibits remarkable electrical, optical, and chemical properties [9–11]. Additionally, its non-toxicity and abundance on Earth make it an ideal candidate for numerous uses, including gas sensors [12] , solar cells [13], energy storage devices [14], transparent conductive films [15], catalysts [16].

SnO_2 is an intrinsically transparent n-type semiconductor, crystallized in the tetragonal rutile structure (space group P_{42}/mm) with lattice parameters a=b=4.7397 Å, c=3.1877 Å and $\alpha = \beta = \gamma = 90°$ [17], and a wide direct bandgap of 3.6 eV [18–21]. SnO2 is appropriate for optoelectronic applications because of its wide bandgap, which enables it to maintain conductivity while being transparent to visible light [22,23]. Doping SnO2 with foreign elements or impurities has been the subject of recent developments in order to change its electronic structure, increase conductivity, and improve performance in a variety of applications.

Calculations using Density Functional Theory (DFT) are now necessary to comprehend the electronic structure and characteristics of materials at the atomic level. DFT calculations shed important light on the electronic band structure, charge distribution, and optical characteristics of SnO2. With excellent precision, researchers can predict material behavior by simulating SnO2 under various situations. Our study aims to investigate the structural and optoelectronic properties of

* Corresponding author: mhalla.jaouad@uit.ac.ma
https://doi.org/10.15251/DJNB.2024.194.1677

$Sn_{0.92}TM_{0.08}O_2$ based on first-principles calculations within the framework of density functional theory (DFT), as implemented in the Quantum Espresso package [24,25], using a plane-wave basis set and the projector-augmented wave method. We employed the generalized gradient approximation (GGA) developed by Perdew, Burke, and Ernzerhof (PBE) [26] for electron exchange-correlation functionals. Additionally, we conducted DFT+U calculations to determine the optimal Hubbard parameters and starting spin polarization for studying the electronic and optical properties of $Sn_{0.92}TM_{0.08}O_2$, where TM represents Fe, Co, and Ni.

2. Computational details

All computations were performed utilizing the Quantum Espresso (QE) software tool within the context of density functional theory (DFT). [24]. This package implements the plane-wave basis set along with the projector-augmented wave (PAW) method [27]. For the electron exchange and correlation functions, we adopted the generalized gradient approximation (GGA) [26].

We constructed a supercell with dimensions 3 × 2 × 1, as illustrated in Fig. 1. In this supercell, we performed substitutional doping by replacing a tin (Sn) atom located at the original position (0, 0, 0) with a transition metal (TM) atom, achieving a doping concentration of 08%.

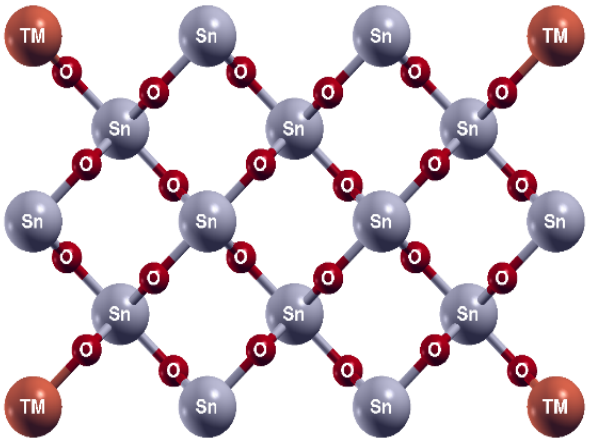

Fig. 1. The 3 × 2 × 1 supercell of the $Sn_{0.92}TM_{0.08}O_2$ with TM = Fe, Co, Ni.

Structural optimization was performed on both undoped and doped supercells. This process included determining the optimal starting spin polarization and was carried out until the force on each atom was minimized to less than 0.001 Ry/Bohr. The kinetic energy cutoff for the plane wave expansion was set to 637.306 Ry, and the cutoff for charge density and potential was set to 70.811 Ry.

For the electron-ion interactions, we employed the scalar relativistic Rappe Rabe Kaxiras Joannopoulos ultrasoft (RRKJUS) pseudopotentials [28] in all calculations, with the exception of optical property calculations. For these, we utilized norm-conserving pseudopotentials (NCPP) [29,30] to ensure accuracy.

3. Results and discussion

3.1. Investigation of Hubbard parameters U

We performed Density Functional Theory (DFT) calculations enhanced with the Hubbard U correction (DFT+U) to investigate the electronic properties of undoped tin dioxide (SnO_2). The focus was on accurately determining the bandgap energy (E_g) of the material by systematically

adjusting the Hubbard parameters $U_{Sn\text{-}5p}$ and $U_{O\text{-}2p}$ over a range from 0.1 eV to 10 eV. Our goal was to find a combination of these parameters that yields a calculated bandgap consistent with the experimentally reported value of 3.6 eV. We prepared the initial crystal structure of SnO_2 using known lattice parameters [17] and performed electronic structure calculations using the DFT+U approach for each pair of $U_{Sn\text{-}5p}$ and $U_{O\text{-}2p}$ within the specified range. The bandgap E_g was determined as the energy difference between the conduction band minimum (CBM) and the valence band maximum (VBM) for each set of Hubbard parameters and compared with the experimental value. This method allowed us to identify the optimal pairs of Hubbard parameters that produce a bandgap closest to the experimental value. By systematically varying $U_{Sn\text{-}5p}$ and $U_{O\text{-}2p}$, we aim to refine the DFT+U method for SnO_2, improving its predictive accuracy for electronic properties such as the bandgap.

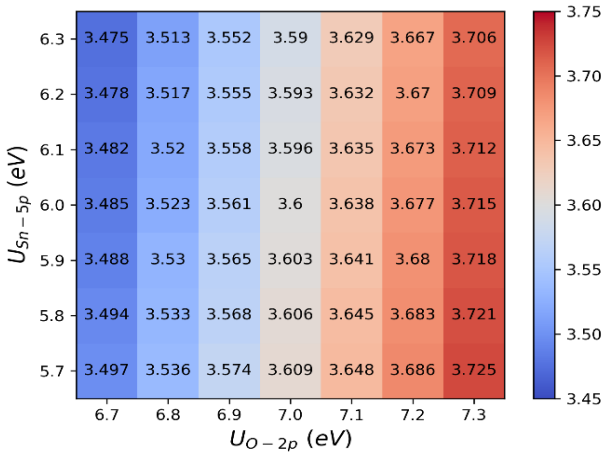

Fig. 2. Variation of bandgap values for several Hubbard parameters $U_{Sn\text{-}5p}$ and $U_{O\text{-}2p}$.

Fig. 2 depicts the variation of bandgap values as a function of the Hubbard parameters $U_{Sn\text{-}5p}$ applied to the Sn-5p orbital and $U_{O\text{-}2p}$ applied to the O-2p orbital. The experimentally reported bandgap energy (E_g=3.6 eV) is achieved with the Hubbard parameters $U_{Sn\text{-}5p}$=6 eV and $U_{O\text{-}2p}$=7 eV. For transition metal (TM) doping elements (TM = Fe, Co, Ni), the Hubbard parameters were set at $U_{Fe\text{-}3d}$=4.6 eV, $U_{Co\text{-}3d}$=5.0 eV, and $U_{Ni\text{-}3d}$=5.1 eV, applied to the $3d$ orbitals of Fe, Co, and Ni, respectively [31]. These optimal Hubbard parameter values were used in all subsequent calculations.

3.2. Investigation of the optimal value of the starting spin polarization

When doping tin dioxide (SnO_2) with a transition metal (TM = Fe, Co, Ni), an additional parameter, the starting spin polarization, needs to be optimized. To explore this, we varied the spin polarization from -1 to 1 in increments of 0.1, aiming to identify the value that results in the minimum energy of the system (see Fig. 3).

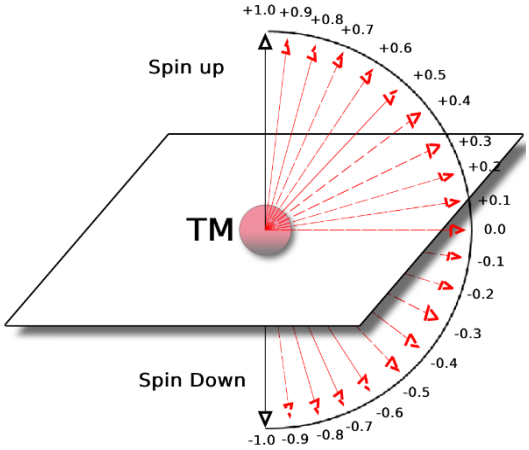

Fig. 3. Illustration of variations of the starting spin polarization of the transition metal in the $Sn_{0.92}TM_{0.08}O_2$.

This investigation was conducted both before and after the relaxation of the material's lattice parameters. The results obtained post-relaxation are presented in Table 1:

Table 1. Optimal values of starting spin polarization after structural relaxation of $Sn_{0.92}TM_{0.08}O_2$.

Starting spin polarization	Total energy of TM-doped SnO_2 (Rydberg)		
	TM = Fe	TM = Co	TM = Ni
-1.0	-2812.51804090	-2856.00764884	-2904.05110857
-0.9	-2812.51804087	-2856.00764819	-2904.32225038
-0.8	-2812.51804096	-2856.00764844	-2904.07842037
-0.7	-2812.51804029	-2856.00764861	-2904.07842029
-0.6	-2812.51804083	-2856.00764874	-2904.07842102
-0.5	-2812.51804110	-2856.00764843	-2904.07842113
-0.4	-2812.51804102	-2855.98959704	-2904.07842112
-0.3	-2812.51804108	-2855.99661462	-2904.07842132
-0.2	-2812.51804056	-2856.02030994	-2904.07842086
-0.1	-2812.51804081	-2855.98966084	-2904.32225103
0.0	-2812.28061288	-2855.94150487	-2904.02414369
0.1	-2812.51804081	-2855.98966085	-2904.32225103
0.2	-2812.51804056	-2856.02030994	-2904.07842086
0.3	-2812.51804108	-2855.99661369	-2904.07842132
0.4	-2812.51804102	-2855.97369976	-2904.07842112
0.5	-2812.51804110	-2856.00764843	-2904.07842113
0.6	-2812.51804083	-2856.00764874	-2904.07842102
0.7	-2812.51804029	-2856.00764861	-2904.07842029
0.8	-2812.51804096	-2856.00764844	-2904.07842037
0.9	-2812.51804087	-2856.00764819	-2904.32225038
1.0	-2812.51804090	-2856.00764884	-2904.00676133

The optimal values of starting spin polarization after the structural relaxation of the material, which yield the minimum energy for $Sn_{0.92}TM_{0.08}O_2$, are ± 0.5 for Fe, ± 0.2 for Co and ± 0.1 for Ni. All of the electronic and optical characteristics covered below have been computed using these values.

3.3. Electronic properties

The density functional theory has been used to predict the electronic properties of undoped tin dioxide SnO_2 and $Sn_{0.92}TM_{0.08}O_2$ (TM = Fe, Co, Ni). To conduct the analysis, we employ DFT calculations to investigate the band structure and density of states (DOS), for both undoped and doped SnO_2 systems.

In the undoped SnO_2, DFT helps to accurately describe its electronic band structure, highlighting the nature of its bandgap, which is crucial for its semiconductor properties. The calculated bandgap, along with the corresponding DOS, provides insights into the intrinsic electronic behavior of the material, including the valence and conduction bands' energy levels.

For the doped systems ($Sn_{0.92}TM_{0.08}O_2$), the introduction of transition metal atoms (Fe, Co, Ni) is expected to significantly alter the electronic properties of SnO_2. DFT calculations enable us to explore these changes in detail.

3.3.1. Band structure

By systematically studying the undoped and doped SnO_2 systems using DFT, we aim to gain a comprehensive understanding of how transition metal doping influences the electronic properties of SnO_2. These insights are not only fundamental for theoretical knowledge but also have practical implications for optimizing SnO_2-based materials for applications in electronics, sensing, and catalysis.

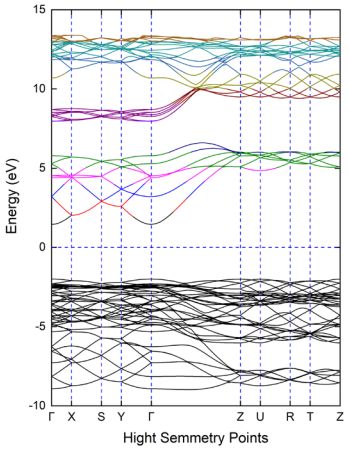

(a) Undoped SnO2

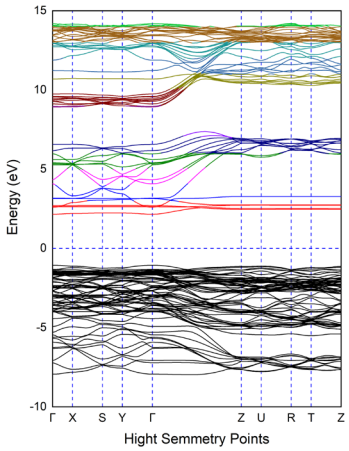

(b) Fe-doped SnO2 (spin up)

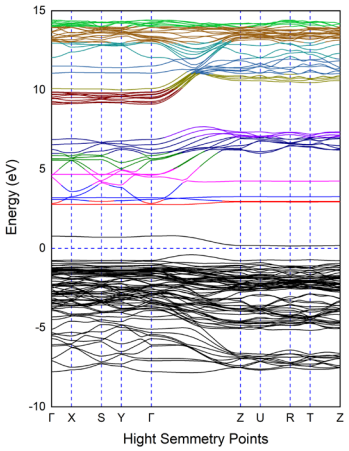

(c) Co-doped SnO2 (spin up)

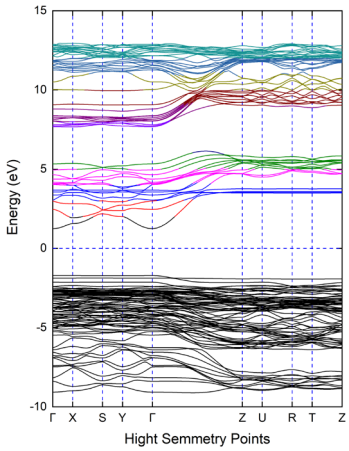

(d) Ni-doped SnO2 (spin up)

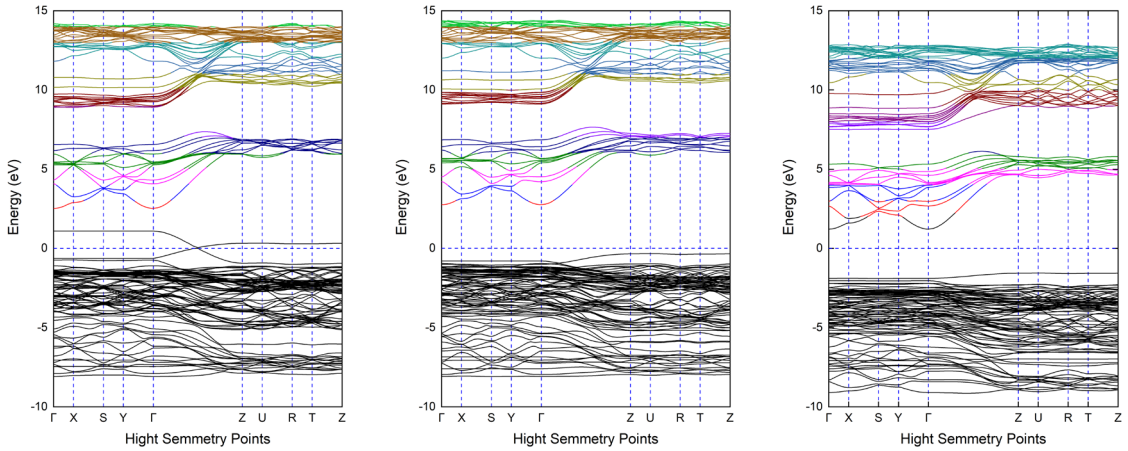

(e) Fe-doped SnO2 (spin down) *(f) Co-doped SnO2 (spin down)* *(g) Ni-doped SnO2 (spin down)*

Fig. 4. The electronic band structure of undoped and $Sn_{0.92}TM_{0.08}O_2$ (TM = Fe, Co, Ni) for the spin up and down.

Fig. 4 present the electronic band structures of undoped (Fig. 4.a) and $Sn_{0.92}TM_{0.08}O_2$ (TM = Fe, Co, Ni) (Fig. 4.b-c-d-e-f-g). The electronic band structure of undoped SnO_2 indicates that it is a direct bandgap semiconductor with a bandgap of 3.6 eV occurring at the Γ–Γ symmetry point. This wide bandgap is typical for materials used in optoelectronic applications as it allows the material to be transparent to visible light.

For Fe-doped SnO_2, the spin-up (Fig. 4.b) and spin-down (Fig. 4.e) band structures states reveal that the introduction of Fe atoms creates states within the bandgap of SnO_2, significantly affecting the material's electronic properties. The Fermi level shifts, indicating a transition from an intrinsic n-type semiconductor to a p-type diluted magnetic semiconductor. Similarly, Co-doped SnO_2 band structures also exhibit spin-up (Fig. 4.c) and spin-down (Fig. 4.f) states, with Co doping introducing additional states in the bandgap and shifting the Fermi level. This modification suggests potential applications in spintronics due to the magnetic nature of Co.

Ni-doped SnO_2 shows comparable behavior with separate band structures for spin-up (Fig. 4.d) and spin-down (Fig. 4.g) states. The introduction of Ni doping also creates additional states within the bandgap, altering the electronic properties and shifting the Fermi level.

Doping with transition metals (Fe, Co, Ni) results in a reduction of the bandgap compared to undoped SnO_2, attributed to the introduction of new electronic states within the bandgap. The band structures for doped SnO_2 indicate spin polarization, highlighting the magnetic nature of these doped materials, particularly in the split of the spin-up and spin-down states. The shift in the Fermi level with doping indicates a change in the type of semiconductor from n-type to p-type.

3.3.2. Density of states (DOS)

The density of States (DOS) calculations provides detailed information on the energy levels and the contribution of each dopant to the electronic states near the Fermi level, which is crucial for understanding changes in conductivity and carrier concentration.

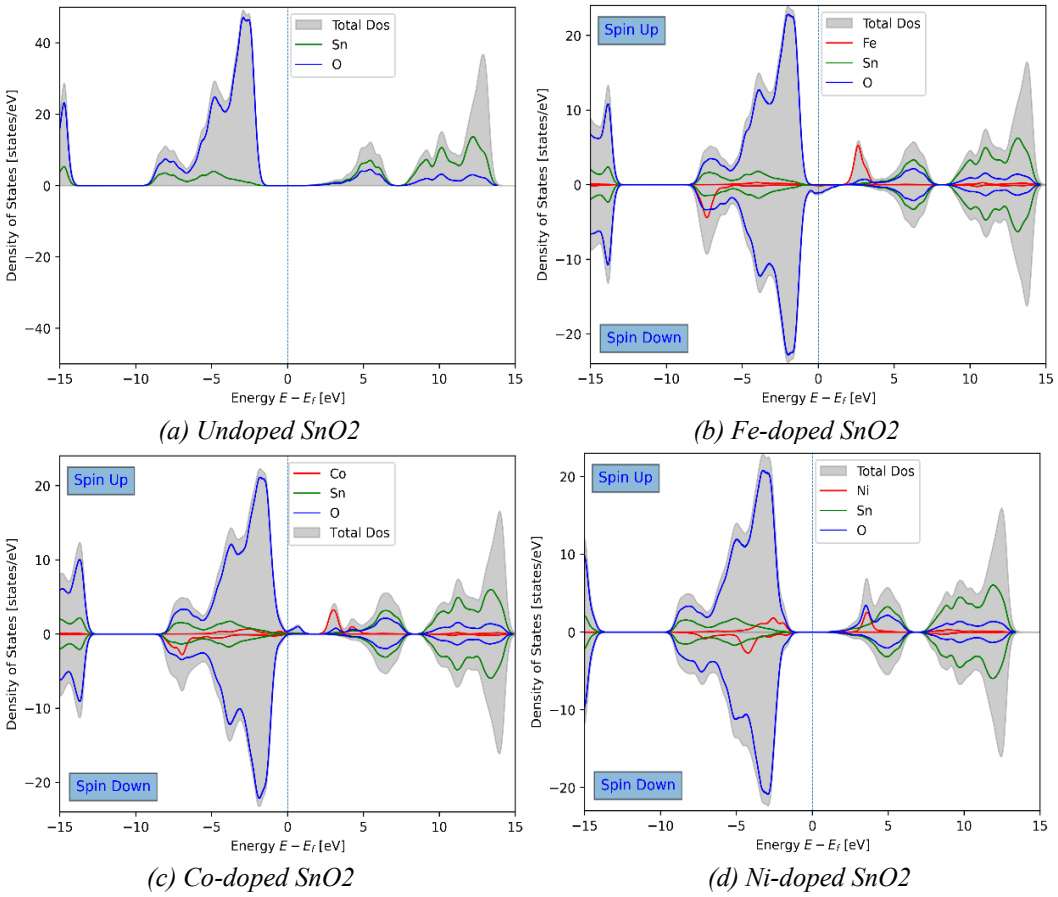

(a) Undoped SnO2 *(b) Fe-doped SnO2*

(c) Co-doped SnO2 *(d) Ni-doped SnO2*

Fig. 5. The total density of states of undoped and $Sn_{0.92}TM_{0.08}O_2$ (TM = Fe, Co, Ni).

Fig. 5 reveals significant changes in the electronic properties of SnO_2 upon doping with transition metals (TM = Fe, Co, Ni):

In undoped SnO_2, the DOS displays a distinct separation between the valence and conduction bands, with the Fermi level positioned within the band gap. This indicates typical semiconducting behavior with a wide band gap, as there are no states present in the gap itself.

Upon doping with Fe, additional electronic bound states emerge within the band gap for both spin-up and spin-down configurations. This introduces magnetic characteristics and shifts the Fermi level towards these new states, resulting in a narrower band gap and suggesting a transition towards p-type semiconductor behavior. Similarly, Co doping introduces bound states in the band gap for both spin orientations. The presence of these states and the corresponding Fermi level shift indicate a reduction in the band gap and highlight the potential for spintronic applications due to the magnetic nature of the Co-doped system.

Ni-doped SnO_2 also exhibits additional bound states within the band gap, similar to the effects observed with Fe and Co doping. The DOS shows a shift in the Fermi level, indicating altered electronic properties and a possible transition towards p-type behavior.

3.4. Optical properties

According to equation (1), the complex dielectric function describes the behavior of the material at a photon energy of (hv) [32,33]:

$$\tilde{\varepsilon}(\omega) = \varepsilon_1(\omega) + i\varepsilon_2(\omega) \tag{1}$$

The real part, $\varepsilon_1(\omega)$, which represents the medium's polarization, can be calculated using the Kramers-Kronig relations [34]. The imaginary part, $\varepsilon_2(\omega)$, reflects the material's absorption properties and can be obtained from electronic structure calculations [35].

Using the post-processing code $epsilon.x$ from QE, we calculated the real and imaginary components of the dielectric function, the energy loss function $L(\omega)$ and the optical joint density of states. Since our system is anisotropic, its optical properties vary along the three polarization components [36].

3.4.1. The dielectric function

When light interacts with a material, the complex dielectric function provides key insights into this interaction. The real part of the complex dielectric function, $\varepsilon_1(\omega)$, is used to determine electronic polarizability along different directions. In contrast, the imaginary part, $\varepsilon_2(\omega)$, is directly related to light absorption. Our material exhibits anisotropy, as shown by varying dielectric function values along different polarization directions.

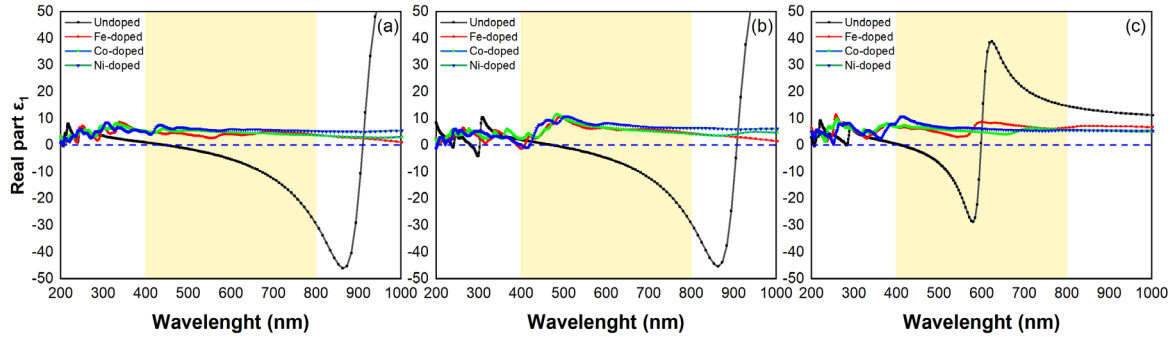

Fig. 6. The real component of the complex dielectric function $\varepsilon(\omega)$ along the directions of (a) x - axis, (b) y - axis, and (c) z - axis for both undoped SnO_2 and $Sn_{0.92}TM_{0.08}O_2$.

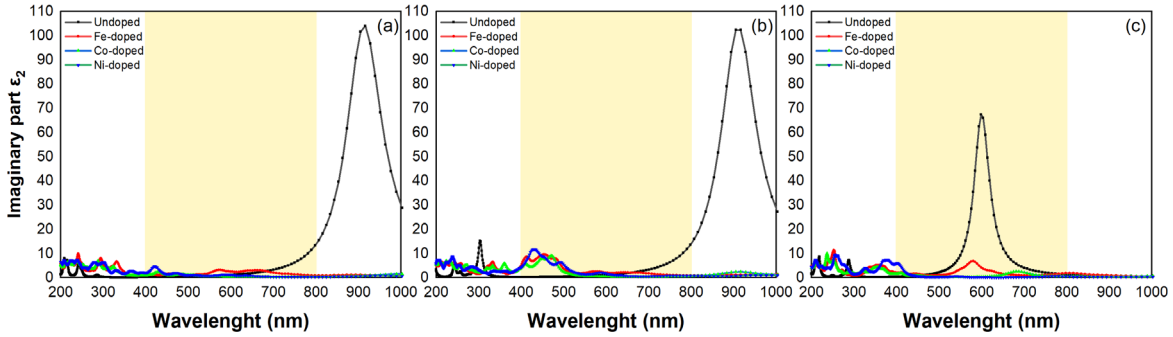

Fig. 7. The imaginary component of the complex dielectric function $\varepsilon(\omega)$ along the directions of (a) x - axis, (b) y - axis, and (c) z - axis for both undoped SnO_2 and $Sn_{0.92}TM_{0.08}O_2$.

Fig. 6 illustrates the real component of the complex dielectric function $\varepsilon(\omega)$ along the x, y, and z axes for both undoped and doped SnO_2. The intense peaks at high wavelengths (~860 nm) along the x and y directions for undoped SnO_2 indicate greater polarizability in the IR region, signifying strong responses to low-energy photons due to low-energy electronic transitions. In contrast, the less intense peak around 600 nm along the z direction suggests some interaction with higher-energy photons in the visible region. $Sn_{0.92}TM_{0.08}O_2$, however, exhibits peaks over a lower wavelength range (200-550 nm), indicating the introduction of new electronic states by the dopants, facilitating higher-energy transitions primarily in the UV-Visible region.

Similarly, Fig. 7, which shows the imaginary component of the dielectric function, reflects these trends. The significant absorption in the IR region along the x and y directions and in the visible region along the z direction for undoped SnO_2 suggests efficient interaction with low-energy and mid-energy photons, respectively. The $Sn_{0.92}TM_{0.08}O_2$'s peaks in the UV-Visible region indicate

the presence of new electronic states introduced by the dopants, enhancing the material's response to higher-energy photons.

3.4.2. The refractive index and extinction coefficient

The complex refractive index, refractive index, and extinction coefficient [37,38] are mathematically expressed as follows:

$$\tilde{n}(\omega) = n(\omega) + ik(\omega) \tag{2}$$

where,

$$n(\omega) = \frac{1}{\sqrt{2}}\left[\sqrt{\{\varepsilon_1^2(\omega) + \varepsilon_2^2(\omega)\}} + \varepsilon_{1(\omega)}\right]^{\frac{1}{2}} \quad \text{and} \quad k(\omega) = \frac{1}{\sqrt{2}}\left[\sqrt{\{\varepsilon_1^2(\omega) + \varepsilon_2^2(\omega)\}} - \varepsilon_{1(\omega)}\right]^{\frac{1}{2}} \tag{3}$$

The refractive index $n(\omega)$ and extinction coefficient $k(\omega)$ of undoped and $Sn_{0.92}TM_{0.08}O_2$ were calculated and used to study the propagation of light in the material.

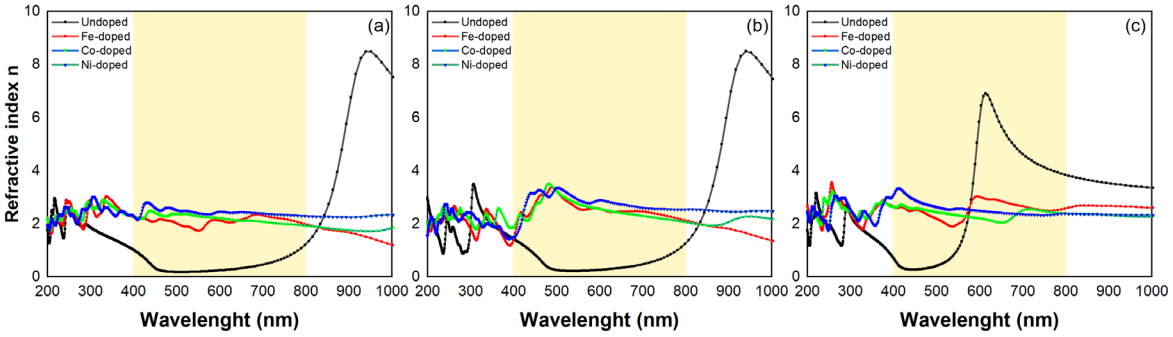

Fig. 8. The refractive index n(ω) for undoped SnO_2 and $Sn_{0.92}TM_{0.08}O_2$ along different directions of polarization: (a) x - axis (b) y - axis and (c) z - axis.

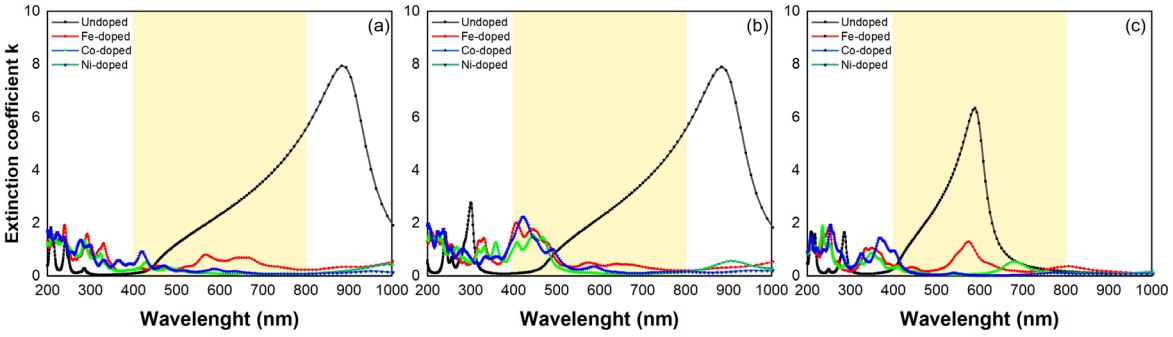

Fig. 9. The extinction coefficient k(ω) for undoped SnO_2 and $Sn_{0.92}TM_{0.08}O_2$ along different directions of polarization: (a) x - axis (b) y - axis and (c) z - axis.

Fig. 8 shows the refractive index $n(\omega)$ of undoped and doped SnO_2 along different polarization directions (x, y, z axes):

For undoped SnO_2, the refractive index demonstrates a significant peak in the IR region, indicating strong dispersion and interaction with low-energy photons. This behavior is consistent with the material's higher polarizability in the IR region. In contrast, doped SnO_2 exhibits a peak in the UV-Visible region, suggesting that doping alters the electronic structure and introduces new energy states, thereby enhancing interaction with higher-energy photons.

Likewise, Fig. 9 presents the extinction coefficient $k(\omega)$ undoped and doped SnO_2 along different polarization directions. The high values of the extinction coefficient in the UV region for both undoped and doped SnO_2 indicate significant interaction with electromagnetic waves at these energies, corresponding to increased optical density. In doped SnO_2, the progressive increase in the extinction coefficient in the visible region suggests that doping introduces additional bound states, enhancing the material's ability to attenuate light at lower energies compared to undoped SnO_2.

3.4.3. The absorption coefficient

The optical absorption coefficient provides a measure of the intensity of the photon energy that the material absorbs. The absorption coefficient $\alpha(\omega)$ was calculated as follows [39]:

$$\alpha(\omega) = \frac{4\pi}{\lambda} k(\omega) \tag{4}$$

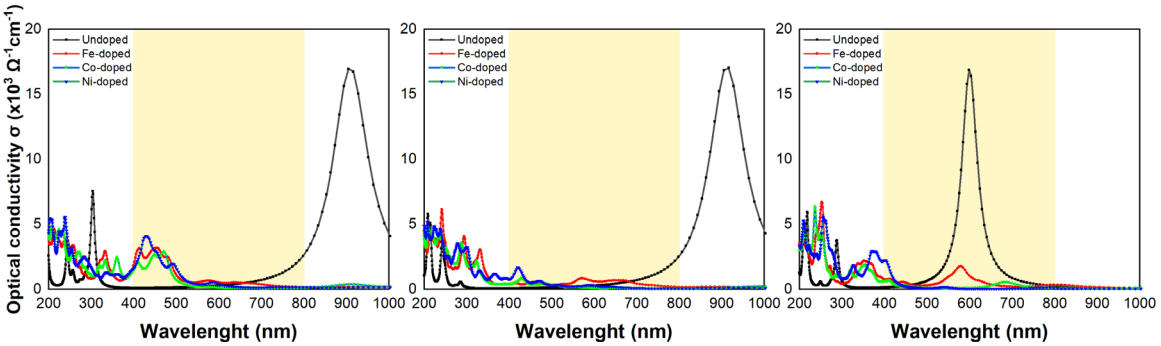

Fig. 10. The absorption coefficient $\alpha(\omega)$ for undoped SnO_2 and $Sn_{0.92}TM_{0.08}O_2$ along different directions of polarization: (a) x - axis (b) y - axis and (c) z - axis.

The absorption coefficient $\alpha(\omega)$, depicted in Fig. 10, shows distinct behaviors along the x-axis, y-axis, and z-axis for both undoped and doped SnO_2. In undoped SnO_2, strong absorption is observed in the UV region across all three polarization directions, indicating primary interactions with higher-energy photons. The absorption is weaker in the visible region, suggesting less interaction with lower-energy photons. The increased absorption in the IR region can be attributed to free carrier absorption.

For doped SnO_2, high absorption in the UV and early visible regions along all polarization axes points to the presence of new energy levels introduced by the dopants, which facilitate the absorption of lower-energy photons and enhance overall absorption. This enhanced absorption is consistent across the x, y, and z polarization directions, indicating that the dopants uniformly affect the electronic structure regardless of the polarization direction.

3.4.4. Reflectivity spectra

The reflectivity $R(\omega)$ of the undoped and $Sn_{0.92}TM_{0.08}O_2$ is given by the following expression [40]:

$$R(\omega) = \frac{(1-n(\omega))^2 + k(\omega)^2}{(1+n(\omega))^2 + k(\omega)^2} \tag{5}$$

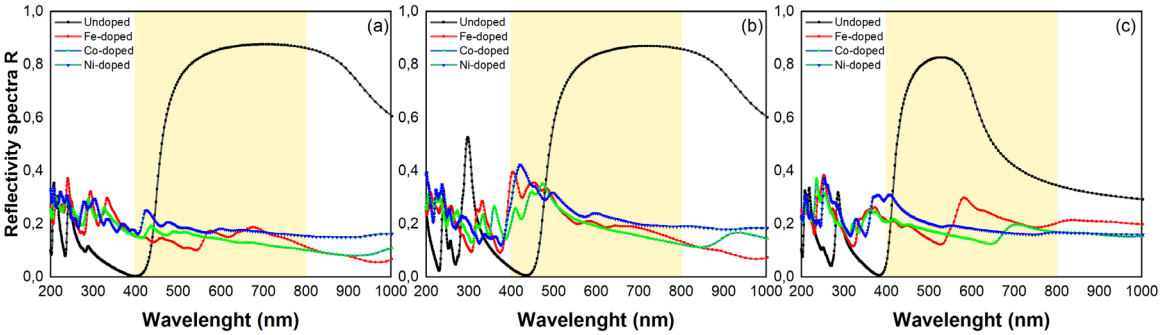

Fig. 11. The reflectivity spectra R(ω) for undoped SnO_2 and $Sn_{0.92}TM_{0.08}O_2$ along different directions of polarization: (a) x - axis (b) y - axis and (c) z - axis.

Fig. 11 illustrates the reflectivity spectra $R(\omega)$ along different polarization directions. The low reflectivity in the UV region for undoped SnO_2 suggests efficient absorption of UV light across all polarization axes, consistent with the strong absorption observed in the UV region. Higher reflectivity in the visible and IR regions indicates minimal interaction with these photons. For doped SnO_2, reduced reflectivity in the UV region, and progressively in the visible and IR regions along the x-axis, y-axis, and z-axis, implies that the dopants create new electronic states that absorb more light, thus reducing reflectivity uniformly across all polarization directions.

3.4.5. The optical conductivity

The optical conductivity $\sigma_{opt}(\omega)$ is calculated along the three polarization components by the following expression [41]:

$$\sigma_{opt}(\omega) = \frac{c}{4\pi}\alpha(\omega)n(\omega) \tag{6}$$

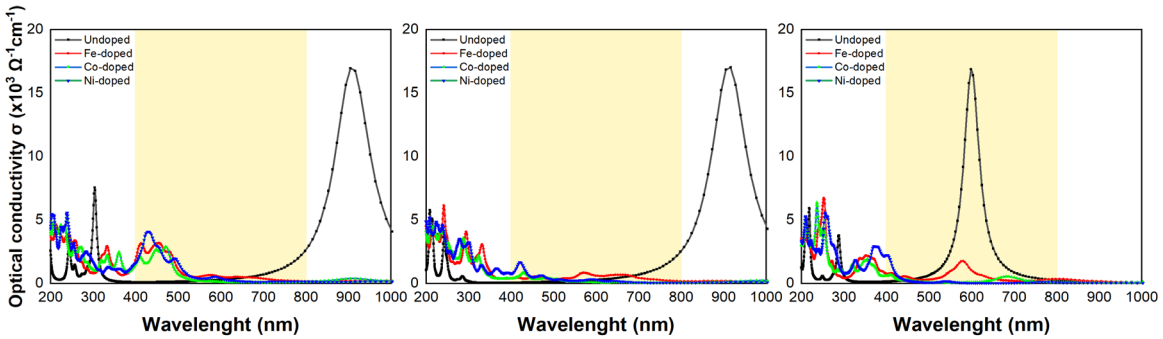

Fig. 12. The optical conductivity $\sigma_{opt}(\omega)$ for undoped SnO_2 and $Sn_{0.92}TM_{0.08}O_2$ along different directions of polarization: (a) x - axis (b) y - axis and (c) z - axis.

The optical conductivity $\sigma_{opt}(\omega)$ shown in Fig. 12 measures the material's ability to conduct electric current under an optical field. The peaks in the UV region for undoped SnO_2 indicate strong electronic transitions and possible interband transitions. The additional peaks in the UV and early visible regions for doped SnO_2 suggest enhanced conductivity due to the presence of dopants, which introduce new pathways for electron excitation and movement, thereby enhancing overall optical conductivity.

3.4.6. The energy loss function

The energy loss function contains features associated with the excitation of the solid's valence electrons. These include interband and intraband transitions, as well as plasmonic excitation. The energy loss function $L(\omega)$ along the three polarization components is depicted in Fig. 13 [42].

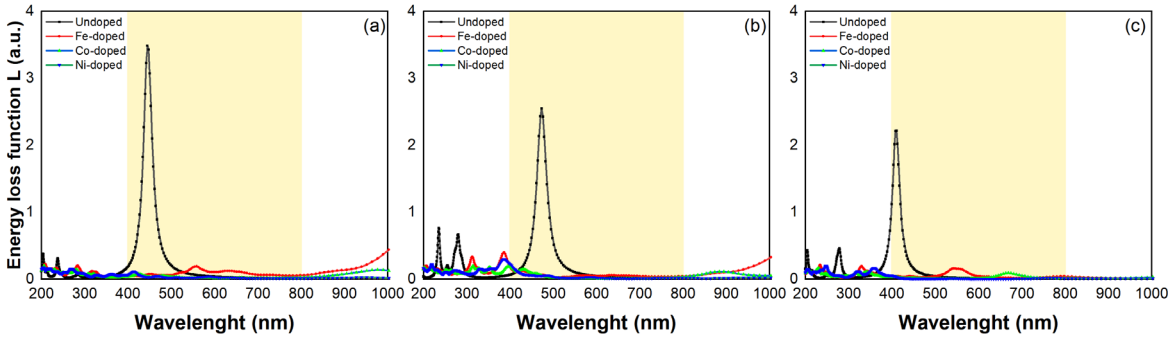

Fig. 13. The energy loss function L(ω) for undoped SnO_2 and $Sn_{0.92}TM_{0.08}O_2$ along different directions of polarization: (a) x - axis (b) y - axis and (c) z - axis.

Fig. 13, which depicts the energy loss function $L(\omega)$, reveals resonances associated with plasmon oscillations in the visible region for undoped SnO_2, with sharp peaks indicating significant changes in the reflectivity spectra. The shifts in these peaks for doped SnO_2 suggest alterations in the plasmonic behavior due to the introduction of dopants, which modify the electronic environment and alter the energy loss characteristics.

3.4.7. The optical joint density of states

The optical joint density of states (JDOS) represents the number of electronic states available for optical transitions at a given energy and provides insight into the interaction of photons with electronic states in the material [43].

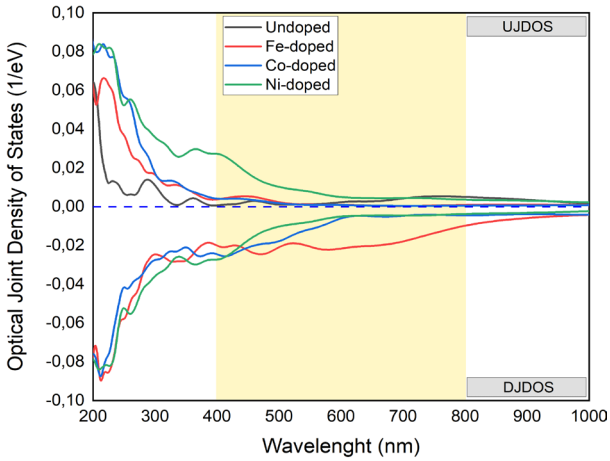

Fig. 14. The optical joint density of states (JDOS) for the undoped SnO_2 and the $Sn_{0.92}TM_{0.08}O_2$.

Fig. 14 illustrates the optical joint density of states (JDOS) for undoped SnO_2 and $Sn_{0.92}TM_{0.08}O_2$ (where TM = Fe, Co, Ni).

For undoped SnO_2, the JDOS shows significant peaks in the UV region, indicating a high density of states available for optical transitions at these energies. This suggests that undoped SnO_2 is more responsive to high-energy photons in the UV range, which correlates with strong absorption observed in this region.

In contrast, the doped SnO_2 ($Sn_{0.92}TM_{0.08}O_2$) exhibits additional peaks in the visible region along with the UV region. This implies that the introduction of transition metal dopants (Fe, Co, Ni) creates new electronic bound states that facilitate optical transitions at lower energies (visible range).

Consequently, doped SnO_2 materials are likely to absorb a broader spectrum of light, including both UV and visible regions, enhancing their overall optical response.

Overall, the JDOS analysis confirms that doping SnO_2 with transition metals modifies its electronic structure, introducing new states that allow for increased optical activity across a wider range of photon energies. This is consistent with the observed absorption and reflectivity spectra discussed earlier

4. Conclusion

In summary, this study has systematically explored the electronic and optical properties of SnO_2 and its transition metal (TM)-doped variants (TM = Fe, Co, Ni) employing first-principles calculations based on the density functional theory (DFT) framework. Our investigation, conducted with a 08% concentration of TM doping, revealed significant alterations in the electronic band structure and optical properties upon TM doping.

Our results highlight the role of the Hubbard U parameter and starting spin polarization in accurately predicting the properties of these doped systems. The optimal values for these parameters were determined, ensuring the reliability of our computational approach.

The undoped SnO_2 displayed a wide direct bandgap of 3.6 eV, confirming its n-type semiconductor nature. However, substitutional doping with Fe, Co, and Ni introduced mid-gap bound states, transforming SnO_2 into a diluted magnetic semiconductor (DMS) with a direct bandgap. This change in the electronic structure is attributed to the interaction between the dopant 3d orbitals and the SnO_2 matrix, which results in the modification of the density of states (DOS) and the Fermi level positioning.

Optically, TM doping significantly impacted the dielectric function, refractive index, absorption coefficient, and energy loss function. The doped systems exhibited enhanced absorption in the UV-visible region, with a noticeable shift in peak intensities. Co and Ni doping showed the highest intraband transition contributions, indicating their potential for applications in optoelectronic devices and transparent conducting electrodes.

This comprehensive investigation provides a deeper understanding of the fundamental properties of TM-doped SnO_2, paving the way for their application in advanced photonic and optoelectronic devices. The findings not only advance the knowledge of DMS materials but also open up new possibilities for the development of high-performance, transparent conducting materials.

References

[1] H. Liu, V. Avrutin, N. Izyumskaya, Ü. Özgür, H. Morkoç, Superlattices and Microstructures **48** (5), 458–484 (2010); https://doi.org/10.1016/j.spmi.2010.08.011
[2] Y. Yang, S. Li, F. Liu, N. Zhang, K. Liu, S. Wang, G. Fang, Journal of Luminescence **186**, 223–228 (2017); https://doi.org/10.1016/j.jlumin.2017.02.043
[3] R. Mahanta, P. Chetri, D. Bora, Materials Today: Proceedings (2023); https://doi.org/10.1016/j.matpr.2023.04.348
[4] R. L. Hoye, K. P. Musselman, J. L. MacManus-Driscoll, APL materials **1** (6) (2013); https://doi.org/10.1063/1.4833475
[5] A. Benhaoua, A. Rahal, B. Benhaoua, and M. Jlassi, Superlattices and Microstructures **70**, 61 (2014); https://doi.org/10.1016/j.spmi.2014.02.005
[6] W. Gong, G. Wang, Y. Gong, L. Zhao, L. Mo, H. Diao, H. Tian, W. Wang, J. Zong, W. Wang, Solar Energy Materials and Solar Cells **234**, 111404 (2022); https://doi.org/10.1016/j.solmat.2021.111404
[7] Y. Kumar, H. S. Akkera, G. S. Reddy, N. Kambhala, Physica B: Condensed Matter **683**, 415881 (2024); https://doi.org/10.1016/j.physb.2024.415881
[8] H. S. Akkera, Y. Kumar, M. D. Kumar, G. S. Reddy, B. R. Kumar, U. M. Pasha, Y. Bitla, V. Ganesh, Optical Materials **133**, 112993 (2022); https://doi.org/10.1016/j.optmat.2022.112993

[9] G. Korotcenkov, S. D. Han, Materials Chemistry and Physics **113**, 756 (2009). https://doi.org/10.1016/j.matchemphys.2008.08.031
[10] R. Narzary, B. Dey, L. Chouhan, S. Kumar, S. Ravi, and S. K. Srivastava, Materials Science in Semiconductor Processing **142**, 106477 (2022); https://doi.org/10.1016/j.mssp.2022.106477
[11] S. K. Srivastava, R. Brahma, S. Datta, S. Guha, Aakansha, S. S. Baro, B. Narzary, D. R. Basumatary, M. Kar, S. Ravi, Mater. Res. Express **6**, 126107 (2019); https://doi.org/10.1088/2053-1591/ab58b1
[12] Q. Zhou, W. Chen, L. Xu, R. Kumar, Y. Gui, Z. Zhao, C. Tang, S. Zhu, Ceramics International **44**, 4392 (2018); https://doi.org/10.1016/j.ceramint.2017.12.038
[13] T. Liu, X. Zhang, J. Zhang, W. Wang, L. Feng, L. Wu, W. Li, G. Zeng, B. Li, International Journal of Photoenergy **2013**, 765938 (2013); https://doi.org/10.1155/2013/765938
[14] X. Chen, S. S. Mao, Chem. Rev. **107**, 2891 (2007); https://doi.org/10.1021/cr0500535
[15] H. J. Kim, U. Kim, T. H. Kim, J. Kim, H. M. Kim, B.-G. Jeon, W.-J. Lee, H. S. Mun, K. T. Hong, J. Yu, K. Char, K. H. Kim, Phys. Rev. B **86**, 165205 (2012); https://doi.org/10.1103/PhysRevB.86.165205
[16] K. T. Ranjit, B. Viswanathan, Journal of Photochemistry and Photobiology A: Chemistry **108**, 79 (1997); https://doi.org/10.1016/S1010-6030(97)00005-1
[17] J. Xu, S. Huang, and Z. Wang, Solid State Communications **149**, 527 (2009); https://doi.org/10.1016/j.ssc.2009.01.010
[18] L. Wang, Y. Wang, K. Yu, S. Wang, Y. Zhang, C. Wei, Sensors and Actuators B: Chemical **232**, 91 (2016); https://doi.org/10.1016/j.snb.2016.02.135
[19] S. Li, Y. Liu, Y. Wu, W. Chen, Z. Qin, N. Gong, D. Yu, Physica B: Condensed Matter **489**, 33 (2016); https://doi.org/10.1016/j.physb.2016.02.021
[20] B. Yuliarto, G. Gumilar, N. L. W. Septiani, Advances in Materials Science and Engineering **2015**, 694823 (2015); https://doi.org/10.1155/2015/694823
[21] A. S. Ahmed, M. Shafeeq M., M. L. Singla, S. Tabassum, A. H. Naqvi, A. Azam, Journal of Luminescence **131**, 1 (2011); https://doi.org/10.1016/j.jlumin.2010.07.017
[22] S. K. Srivastava, P. Lejay, B. Barbara, S. Pailhès, V. Madigou, G. Bouzerar, Phys. Rev. B **82**, 193203 (2010); https://doi.org/10.1103/PhysRevB.82.193203
[23] V. S. Ganesha Krishna, M. G. Mahesha, Journal of Alloys and Compounds **848**, 156568 (2020); https://doi.org/10.1016/j.jallcom.2020.156568
[24] P. Giannozzi, S. Baroni, N. Bonini, M. Calandra, R. Car, C. Cavazzoni, D. Ceresoli, G. L. Chiarotti, M. Cococcioni, I. Dabo, A. D. Corso, S. de Gironcoli, S. Fabris, G. Fratesi, R. Gebauer, U. Gerstmann, C. Gougoussis, A. Kokalj, M. Lazzeri, L. Martin-Samos, N. Marzari, F. Mauri, R. Mazzarello, S. Paolini, A. Pasquarello, L. Paulatto, C. Sbraccia, S. Scandolo, G. Sclauzero, A. P. Seitsonen, A. Smogunov, P. Umari, R. M. Wentzcovitch, J. Phys.: Condens. Matter **21**, 395502 (2009); https://doi.org/10.1088/0953-8984/21/39/395502
[25] P. Giannozzi, O. Andreussi, T. Brumme, O. Bunau, M. B. Nardelli, M. Calandra, R. Car, C. Cavazzoni, D. Ceresoli, M. Cococcioni, et al., Journal of physics: Condensed matter **29** (46), 465901 (2017); https://doi.org/10.1088/1361-648X/aa8f79
[26] J. P. Perdew, K. Burke, M. Ernzerhof, Phys. Rev. Lett. **77**, 3865 (1996); https://doi.org/10.1103/PhysRevLett.77.3865
[27] G. Kresse, D. Joubert, Phys. Rev. B **59**, 1758 (1999); https://doi.org/10.1103/PhysRevB.59.1758
[28] A. M. Rappe, K. M. Rabe, E. Kaxiras, J. D. Joannopoulos, Phys. Rev. B **41**, 1227 (1990); https://doi.org/10.1103/PhysRevB.41.1227
[29] D. Hamann, M. Schlüter, C. Chiang, Physical Review Letters **43** (20), 1494 (1979); https://doi.org/10.1103/PhysRevLett.43.1494
[30] N. Troullier, J. L. Martins, Phys. Rev. B **43**, 1993 (1991); https://doi.org/10.1103/PhysRevB.43.1993
[31] W. Akbar, I. Elahi, S. Nazir, Journal of Magnetism and Magnetic Materials **511**, 166948 (2020); https://doi.org/10.1016/j.jmmm.2020.166948
[32] K. Tanji, I. El Mrabet, Y. Fahoul, A. Soussi, M. Belghiti, I. Jellal, Y. Naciri, A. El Gaidoumi, A. Kherbeche, Reac Kinet Mech Cat **136**, 1125 (2023); https://doi.org/10.1007/s11144-023-02385-0

[33] A. Soussi, A. Elfanaoui, M. Taoufiq, A. Asbayou, L. Boulkaddat, N. Labchir, R. Markazi, A. Ihlal, K. Bouabid, et al., Materials Today Communications **36**, 106520 (2023); https://doi.org/10.1016/j.mtcomm.2023.106520
[34] A. R. Forouhi, I. Bloomer, Phys. Rev. B **38**, 1865 (1988); https://doi.org/10.1103/PhysRevB.38.1865
[35] A. Soussi, A. Ait hssi, L. Boulkaddat, A. Asbayou, N. Labchir, A. Elfanaoui, R. Markazi, K. Bouabid, A. Ihlal, A. Taleb, Physica B: Condensed Matter **643**, 414181 (2022); https://doi.org/10.1016/j.physb.2022.414181
[36] S. Masuda, S. Hosokawa, I. Tochizawa, K. Akutsu, K. Kuwano, A. Iwata, IEEE Transactions on Industry Applications **30**, 377 (1994); https://doi.org/10.1109/28.287520
[37] R. Khan, K. U. Rahman, Q. Zhang, A. U. Rahman, S. Azam, A. Dahshan, Journal of Physics: Condensed Matter **34**, (6) 065502 (2021); https://doi.org/10.1088/1361-648X/ac3583
[38] S. Cheon, K. D. Kihm, H. goo Kim, G. Lim, J. S. Park, J. S. Lee, Sci Rep **4**, 6364 (2014); https://doi.org/10.1038/srep06364
[39] N. V. Smith, Phys. Rev. B **3**, 1862 (1971); https://doi.org/10.1103/PhysRevB.3.1862
[40] R. Khan, M. Aamer, Q. Zhang, N. Ali, S. Azam, A. U. Rahman, M. F. Nasir, I. Qasim, S. Aftab, R. Neffati, M. Amami, Journal of Solid State Chemistry **326**, 124193 (2023); https://doi.org/10.1016/j.jssc.2023.124193
[41] D. Sahoo, P. Priyadarshini, R. Dandela, D. Alagarasan, R. Ganesan, S. Varadharajaperumal, R. Naik, RSC Advances **11**, 16015 (2021); https://doi.org/10.1039/D1RA02368C
[42] A. Otero-de-la Roza, E. R. Johnson, V. Luaña, Computer Physics Communications **185**, (3) 1007–1018 (2014); https://doi.org/10.1016/j.cpc.2013.10.026
[43] K. Balakrishnan, V. Veerapandy, P. Vajeeston, Computational Condensed Matter **37**, e00856 (2023); https://doi.org/10.1016/j.cocom.2023.e00856